Applied Acoustics 199 (2022) 108989

Contents lists available at ScienceDirect

Applied Acoustics

journal homepage: www.elsevier.com/locate/apacoust

Acoustic wall treatments for wind tunnel aeroacoustic measurements

Hugo F.M. Bento *, Daniele Ragni, Francesco Avallone, Dick Simons, Mirjam Snellen

Faculty of Aerospace, Delft University of Technology, Delft 2629HS, The Netherlands

ARTICLE INFO

Article history:
Received 6 October 2021
Received in revised form 24 May 2022
Accepted 14 August 2022
Available online 2 September 2022

2010 MSC:
00-01
99-00

Keywords:
Sound absorbing materials
Boundary layer
Aerodynamic noise
Geometric modelling
Beamforming

ABSTRACT

Sound absorbing porous materials are used to line a wind tunnel wall, in order to reduce reflections. However, the lining can have a detrimental effect on the acoustic measurements due to an increase in the noise radiated from the walls. In addition, the aerodynamic fidelity of the tunnel can be affected. In the present study, the influence of the porous materials on the boundary layer aerodynamic characteristics is assessed. The consequent aerodynamic noise scattering is also studied, and compared against the acoustic benefit from absorbing reflections in the test section. Geometric modelling is used to understand the influence of varying absorbing materials in reducing the acoustic interference caused by the reflections. The aerodynamic and acoustic results are related to the roughness, and to the viscous and inertial resistivities of the three porous materials studied. The material with highest roughness (polyester wool) is found to result in the strongest turbulent fluctuations in the boundary layer. However, it is the material with the thickest fibre diameter (PU foam), and consequent highest inertial resistivity, which generates the strongest surface noise scattering. Materials with high viscous resistivity, together with low inertial resistivity, are found to provide good sound absorbing capabilities. The results therefore indicate that the best choice of sound absorbing wall treatment for wind tunnel applications results from minimizing roughness and inertial resistivity, while maximizing viscous resistivity.

1. Introduction

Closed wind tunnels are important facilities for aeroacoustic investigations, e.g. of wind turbine blade noise [1,2] or propeller noise [3]. Closed wind tunnels provide a higher aerodynamic fidelity than open-jet tunnels [4]. However, closed wind-tunnels have a typically lower acoustic performance than anechoic open-jet facilities [5]. Reverberation is a major drawback of closed wind tunnels [6]. The challenges of measuring acoustic sources in non free-field conditions is discussed in literature for a wide range of applications, from concert halls [7] to wind tunnels [8]. A possible solution is to reduce the intensity of the reflections during the test, e.g. by applying sound absorbing materials on the walls [9]. A second solution is to use post processing tools which predict the change in response function caused by the reflections, and to account for this change. Furthermore, the use of beamforming techniques can allow for separating a direct acoustic source from its reflections [10]. Measurements taken with a microphone array are typically analysed with beamforming techniques (e.g. [1,8]). However, conventional beamforming resolution is often insufficient to separate reflections from the direct source. The beamforming resolution is particularly low at low frequencies, since it is dictated by the Rayleigh limit [11], highlighting the need to use the two solutions mentioned above. The post-processing approach of modelling the response function of the acoustic measurements, taking into account sound reflections, can be combined with beamforming. Beamforming also allows the increase in signal-to-noise ratio of the source with respect to background noise. In closed wind tunnels, the tunnel walls' boundary layer aerodynamic noise is one of the dominant sources of background noise [12].

Regarding the reflections from wind tunnel walls, geometric modelling can be used to predict reflections in a closed room [13], and therefore to improve beamforming results. Within geometric modelling approaches, the image-source method is simple to implement and helps predicting the propagation of sound in closed spaces [14], reverberation time in a room [15], and also the presence of reflections in a closed wind tunnel test section [16,17]. Guidatti used the prediction from the image-source method in order to apply a reflection canceller, and in this way improve the resulting beamforming maps [18]. More recent studies have also used the image-source method in order to provide theoretical modifications to the Green's function used in the beamforming algorithm [19,16]. The post processing methods discussed

* Corresponding author.
E-mail address: H.F.MouraoBento@tudelft.nl (H.F.M. Bento).

https://doi.org/10.1016/j.apacoust.2022.108989
0003-682X/

in previous studies can be applied to wind tunnel test sections with fully reflective walls, as well as lined walls, by considering the actual reflection coefficient of the walls. However, most of the methods have been tested against experiments with hard-walled wind tunnels. Literature is lacking studies on the applicability of geometric modelling methods, and in particular the image-source method, to the prediction of reflections in lined wind tunnel test sections. The present helps to fulfill this gap, but the main focus is on investigating the effect of the aerodynamic and acoustic properties of the lining materials, on the aerodynamic and acoustic fidelity of a wind tunnel.

Lining a closed wind tunnel with a porous material also affects the aerodynamic characteristics of the wind tunnel walls' boundary layer. The changes in boundary layer profile can affect (closed) wind tunnel aerodynamic corrections, e.g. if the displacement thickness, δ^*, increases and the effective area of the tunnel reduces. Moreover, increases in the turbulence levels in the boundary layer can increase the scattering of spurious noise sources in the tunnel, e.g. from discontinuities [20]. The influence of porous materials on boundary layers is widely studied (e.g. by [21,22]). However, literature is lacking studies with a complete trade-off of lining materials for closed wind tunnels, considering both the aerodynamic changes in the boundary layer, the consequent scattered noise, and the absorption of sound reflections.

Sound absorbing lining materials were tested in the A-Tunnel, at TU Delft. The A-Tunnel is an anechoic open-jet facility, which allows for a reliable characterization of sound sources in the room, from 200 Hz [23]. The wind tunnel models consist of acoustically treated plates, each with its own reflection coefficient. The lining materials also have different surface roughness and flow resistivity. The influence of the lining in the aerodynamic properties of the boundary layer (BL), and, consequently, in the background noise of the tunnel, is characterized. The positive effect of lining the plates is accessed, by analysing the interference between the sound emitted by a known source, with the reflections at each plate. The acoustic measurements are compared against predictions based on geometric modelling. The geometric modelling tool developed in the present study is based on the image source method. For the cases with flow-on, the position of the image source is corrected, in order to take into account the convection of the reflected sound wave.

The methodology followed in the present study is described in Section 2. The section includes a description of the experimental setup, of the measurement techniques and computation methods used, including conventional beamforming and the geometric modelling algorithm used. Section 3 characterises the influence of the lining materials used in the aerodynamic properties of the boundary layer, and consequently on the aerodynamic noise sources in the tunnel, when the flow is on. Sections 4 and 5 show the comparison between experimental results and geometric modelling predictions, for the flow-off case and for the flow-off case, respectively. Finally, Section 6 presents an overview of the findings.

2. Methodology

2.1. Facility and models

The experiment was carried out in the anechoic open-jet wind tunnel (A-Tunnel), at TU Delft. A 40 × 70 cm nozzle was used. With this nozzle, the free-stream turbulence intensity is below 0.1% of the free-stream velocity, U_∞, from 10 ms^{-1} up to the maximum reachable velocity of 35 ms^{-1} [23]. At the bottom of the nozzle, the boundary layer is forced to turbulent by a zigzag trip. A vertical wooden plate was installed on the shorter side of the rectangular nozzle, for the baseline tests (hard-wall case). A smooth transition from the nozzle to the plate was ensured by using tape, in this way removing possible gaps. For the acoustically treated test cases, the smooth plate was lined with sound absorbing materials. Fig. 1 shows that, for the lined plate case, a 0.1 m wooden plate is placed between the nozzle and the start of the lining foam. This wooden plate is flush with the nozzle. The difference in thickness between the 0.1 m wooden plate and each lining leads to a small step, no larger than 3 mm. Fig. 1a shows the plate lined with polyurethane PU foam installed in the A-Tunnel. The microphone array is placed outside the jet, and parallel to the lined plate. As Fig. 1b shows, the speaker was placed 0.25 m outside the jet. The sound source is a miniature QindW speaker, which was verified to have very good omnidirectional characteristics up to 2 kHz. The speaker is placed between the plate and the array, so that the plate is representative of a closed wind tunnel back wall. Fig. 1c indicates the location where flush microphones were installed on the plate. Microphones were installed 1 m downstream of the nozzle, at locations 0 and 1, with z-coordinates 0.02 m and −0.02 m, being $z = 0$ at the plate's spanwise centre. Locations 0c, 0 l, 2 and 3 represent the locations where the flow velocity was measured with hot-wire anemometry. The respective physical coordinates are: (0.46, 0, 0) m, (0.46, 0, 0.045) m, (−0.42, 0, 0) m and (−0.46, 0, 0) m.

Four different plates were tested. In addition to the acoustics, the aerodynamic characteristics of the surface also varied, since the plates have different roughness and resistivities. The baseline plate is a clean wooden plate, which is the most sound reflective test-case. The other 3 models consist of the clean plate lined with melamine foam, polyurethane (PU) foam, and polyester wool. The porous materials are shown in Fig. 2. The roughness of the materials was inferred from 3D scans of the porous surfaces, obtained with a Keyence VR-5000 series microscope. The arithmetical mean height parameter was used for evaluating surface roughness [24]. The flow viscous and inertial resistivities, R_v and R_i, were obtained from permeability tube experiments (setup described in [2]). The main parameters which affect the aerodynamic and acoustic performance of the test plates are summarized in Table 1. Both melamine and wool have very good sound absorption characteristics, whereas PU is more reflective. The sound absorption characteristics of the melamine and wool can be related to their higher viscous resistivity, according to Delany's empirical model [25]. A more detailed characterisation of the acoustic properties of the liners can be found in Section 2.3, where the impedance tube tests are discussed. The high viscous resistivity of the melamine and wool also make the materials less permeable to the incoming flow. The high inertial resistivity of the PU foam is also expected to avoid strong flow velocities inside the material. The polyester wool was the roughest model tested.

2.2. Measurement techniques

The present section describes the measurement techniques used in the experimental campaign. The flow velocity was measured with the hot-wire, the pressure fluctuations on the wall were measured with surface microphones, and the acoustic measurements were made with a free-field phased microphone array.

2.2.1. Flowfield measurements

A Dantec Dynamics hot-wire 55P15 probe was used to measure the streamwise velocity over the plates. The measurements were taken at four locations. Two locations approximately 10 cm the nozzle, locations 2 and 3, and two locations 1 m downstream of the nozzle, locations 0c and 0l (see Fig. 1c). At each location, the boundary layer profiles were taken with a 60 point-distribution, following an exponential function. The distribution of the points provides a higher resolution close to the wall, where the velocity gradients are the highest. The minimum sampling frequency used

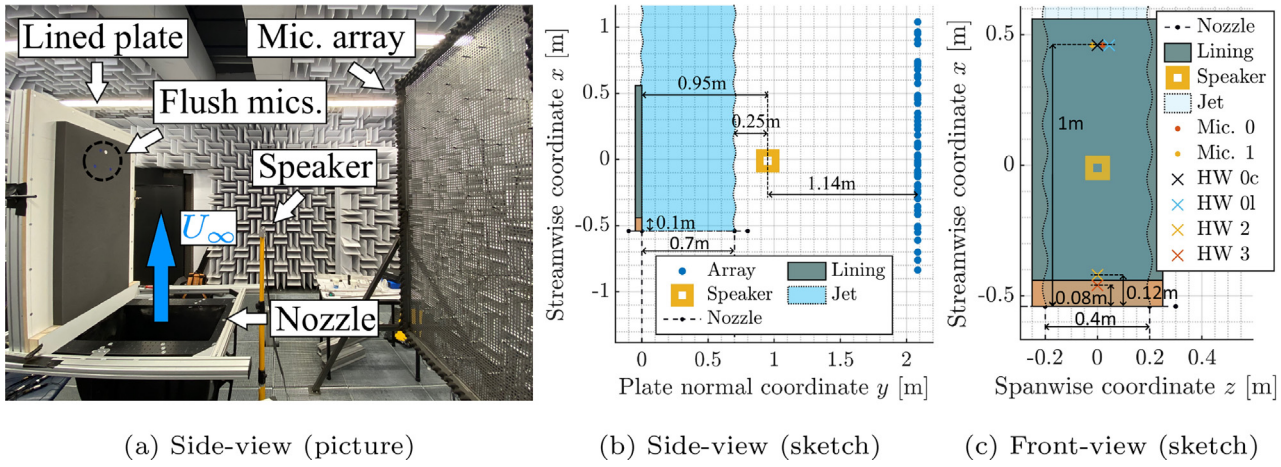

Fig. 1. Experimental setup. Side-view of a lined plate (with PU foam) installed in the anechoic room (left). Representation of the setup with a lined plate: side-view (centre) and front-view (right).

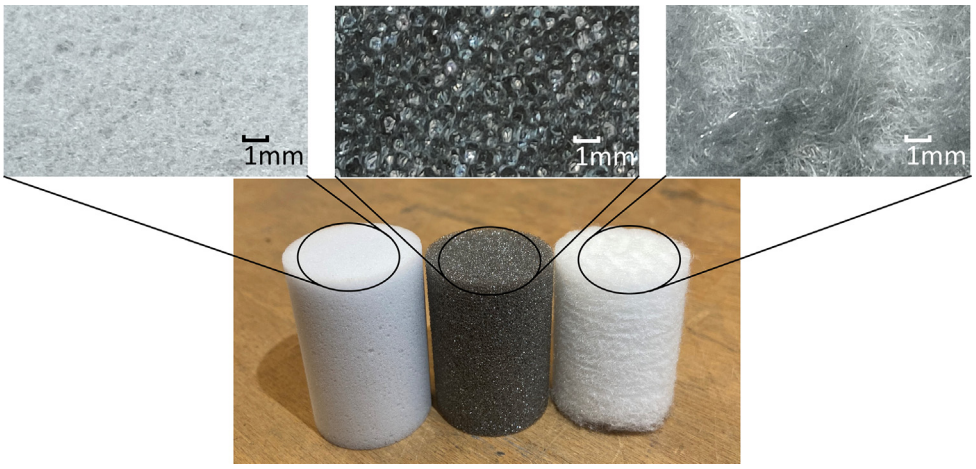

Fig. 2. Samples of melamine foam (left), PU foam (center), and polyester wool (right).

Table 1
Acoustic and aerodynamic properties of the plates tested.

Plate	Average Roughness size	Viscous resistivity R_v [kPa s m^{-2}]	Inertial resistivity R_i [kPa s^2 m^{-3}]
Clean	Low	–	–
Melamine	Medium ($\sim$ 0.1 mm)	9	2
PU	Medium ($\sim$ 0.1 mm)	2	40
Wool	High ($\sim$ 0.6 mm)	8	2

was 25.6 kHz, and the measurement time was 10 s. The velocity measured with the hot-wire was calibrated based on a 4th order polynomial, with respect to the output voltage. A Pitot tube was used as reference, during calibration. The highest source of error in the hot-wire measurements was the temperature variation in the anechoic room. The ambient temperature and pressure were continuously measured, in order to correct for the temperature variations, as discussed in [23]. The repeatability of the results was confirmed by comparing measurements at equal streamwise location, e.g. locations 0c and 0 l.

2.2.2. Wall pressure measurements

The plate was instrumented with a small electret Sonion 8044 microphone, placed at location 0, and a Linear-X M51 microphone, at location 1 (see Fig. 1c). The surface measurements were taken to investigate the magnitude of the surface pressure fluctuations. The Sonion microphone was calibrated with the omnidirectional speaker, and using a reference free-field Linear-X M51 microphone. The Linear-X microphones were calibrated with a G.R.A.S. 42AA pistonphone. The surface microphone measurements were taken with a sampling frequency of 51.2 kHz, and with a measurement time of 20 s.

2.2.3. Free-field acoustic measurements

The free-field acoustic measurements were made with the phased microphone array shown in Fig. 1a. The array consists of 64 G.R.A.S. 40PH free-field microphones. The free-field microphones have an uncertainty of 1 dB, from 50 Hz to 5 kHz [26]. The microphones were calibrated with a G.R.A.S. 42AA pistonphone. The free-field microphone measurements were taken with a sampling frequency of 51.2 kHz, and with a measurement time of 20 s. The location of the microphones in the spiral arms of the array was optimised in order to maximize spatial resolution and minimize side lobe levels in the A-tunnel [27]. The array was placed on the opposite side and parallel to the test plate, so that the mirror source reflection stayed directly behind the speaker, from the point of view of the array.

2.3. Post-processing algorithms

The present section describes the algorithms which were used in the present study. Beamforming was used to estimate the sound

levels of the direct source, with a decreased influence from spurious noise sources. A geometric modelling tool was used to predict the reflections in the experiment.

2.3.1. Conventional beamforming

The measurements from the phased microphone array were post-processed with conventional frequency domain beamforming (CBF). Conventional beamforming is widely used in aeroacoustics research (e.g. in [1,2]), as it is an intuitive and robust method [10]. In CBF, the measured signals of the N microphones in the array are treated in the frequency domain:

$$\boldsymbol{p}(f) = \begin{pmatrix} p'_1(f) \\ \vdots \\ p'_N(f) \end{pmatrix}, \tag{1}$$

being p'_n the pressures recorded at each microphone, n, and f the frequency. The source noise levels, for each grid point, ξ_j, are calculated from:

$$A(\xi_j) = \frac{\boldsymbol{g}_j^*(\boldsymbol{p}\boldsymbol{p}^*)\boldsymbol{g}_j}{\|\boldsymbol{g}_j\|^2}, \tag{2}$$

where $\boldsymbol{p}\boldsymbol{p}^*$ is a $N \times N$ matrix, commonly denoted as cross-spectral matrix (CSM). The asterisk, $(\cdot)^*$, stands for the complex conjugate transpose, and $||\cdot||$ stands for the Euclidean norm of a vector. $\boldsymbol{g}_j$ is the steering vector, which takes into account the phase shift of a sound wave from the grid point to each microphone, n, as well as the geometrical spreading of the wave. In the present formulation, $\boldsymbol{g}_j$ is the Green's function of the sound propagation from a free-field monopole source:

$$g_{j,n} = \frac{\exp\left(-2\pi i f \Delta t_{j,n}\right)}{\|\boldsymbol{x}_n - \xi_j\|} \tag{3}$$

where $\boldsymbol{x}_n$ is a vector containing the positions of the N microphones. $\Delta t_{j,n} = \|\boldsymbol{x}_n - \xi_j\|/c$ is the time the sound wave takes from the grid point ξ_j to the receiver at $\boldsymbol{x}_n$, c being the sound speed.

In the present study, two scan-planes were considered: one including the location of the speaker, and one scan-plane at the plane of the test plate surface. Both planes are parallel to the array. The scan-plane at the test plate location was used in order to characterize the aerodynamic noise sources for the flow-on and speaker-off experimental test cases. For identifying aerodynamic noise sources at the plate, a correction for the convection of sound waves by the flow is applied in the formulation, as described in [28]. The aerodynamic noise sources were analysed for the test cases at the free-stream velocity, U_∞, of 30 ms^{-1}.

For estimating the speaker noise levels from the resulting beamforming map, the Source Power Integration (SPI) method outlined by Sijtsma [28] is applied. The SPI method compares the experimental CSM with the CSM of a simulated point monopole source, with known noise levels, in order to quantify, with a single number, the noise levels of the experimental source:

$$A_{\mathrm{SPI}}(f) = \frac{\sum_{j=1}^{K} \boldsymbol{g}_j^*(\boldsymbol{p}\boldsymbol{p}^*)_{\mathrm{exp.}}\boldsymbol{g}_j}{\sum_{j=1}^{K} \boldsymbol{g}_j^*(\boldsymbol{p}\boldsymbol{p}^*)_{\mathrm{sim.}}\boldsymbol{g}_j}. \tag{4}$$

2.3.2. Acoustic geometric modelling tool

The experimental acoustic results were compared against a geometric modelling tool. The tool assumes that the reflections at the test plate are specular, i.e. neglects the existence of diffuse reflections. It is assumed that the plate is infinite, neglecting the existence of diffraction over the corners of the plate, or over other elements present in the room (e.g. wind tunnel nozzle). With the present assumptions, and with the reflection coefficient of the plates, it is possible to apply the image-source method to predict the effect of reflections at the receiver location [13]. The conventional image-source method does not take into account the convection of the sound wave by the tunnel jet. For the flow-on cases, the path of each sound ray from the mirror source to the receivers (microphones) is re-calculated taking into account convection by the flow. The method, used to calculate the path of the sound ray, resembles the ray tracing technique discussed by Savioja [13]. However, since a single reflective wall is considered, the number of reflections to be calculated equals the number of receivers. The modelling tool is deterministic (as in the mirror source method), in contrast with the widely used stochastic ray tracing techniques. Fig. 3 shows the baseline result of the simulations with the geometric modelling tool. Fig. 3a and b show the prediction of the path of the sound rays, from mirror-source to receiver, for the flow-off and -on cases. For the flow-on cases, the perceived location of the mirror-source is above its flow-off location, and is dependent of receiver position. Fig. 3c shows the predicted spectra, as perceived at the location of the microphone at the centre of the array, for the cases with and without a reflective plate. The spectra are shown as sound pressure levels,

$$\mathrm{SPL} = 20\log_{10}\left(\frac{p'_{\mathrm{rms}}}{p_{\mathrm{ref.}}}\right), \tag{5}$$

with p'_{rms} the root mean square of the pressure fluctuations, and $p_{\mathrm{ref.}}$ the reference pressure, 2×10^{-5} Pa. The difference (in dB) between the two spectra shown in Fig. 3c is considered in the following sections as the measure of the acoustic interference caused by the test plate reflections, for both experimental and simulated microphone signals, at the receiver location. The acoustic interference is therefore estimated from the difference between the spectra measured with an installed plate and the spectra obtained from the measurement with the speaker in a free-field configuration, i.e. without any installed plate:

$$\Delta\mathrm{SPL} = \mathrm{SPL}_{\mathrm{Testcase}} - \mathrm{SPL}_{\mathrm{Free-fieldspeaker}}. \tag{6}$$

Positive and negative peaks in ΔSPL are indicative of, respectively, constructive and destructive interference between the direct and reflected sound waves. The geometric modelling algorithm is validated for frequencies in the range 0.3 kHz to 2 kHz, where the speaker is omnidirectional. The speaker omnidirectionality was verified with measurements of the speaker in the empty A-Tunnel room. The measurements were taken with the speaker at constant distance from the array (≈ 1 m), and for different speaker orientations: 0°, 45°, 90° and 180°. The speaker was rotated with respect to a vertical axis aligned with the speaker's support (see Fig. 1a).

In order to predict the propagation of reflections with a mirror-source algorithm, it is essential to consider the complex valued impedance of the material [29]. The complex reflection coefficient, $\underline{R}$, of the lined plates was calculated based on surface impedance, $\underline{Z}_s$ [29]:

$$\underline{R}(f,\theta_0) = \frac{\underline{Z}_s(f) - Z_0/\cos\theta_0}{\underline{Z}_s(f) + Z_0/\cos\theta_0}, \tag{7}$$

with θ_0 the specular reflection angle, and Z_0 the impedance of air. The surface impedance was estimated based on normal-incidence impedance tests, which were carried out at the Netherlands Aerospace Centre (NLR). In the impedance tube tests, the samples were placed in front of a (fully reflective) solid wall, as in the two microphones' impedance tube setup described in [30]. Fig. 4a shows the absolute R_c, and Fig. 4b shows the phase shift which occurs at the moment of the reflection. Fig. 4 also shows the prediction based

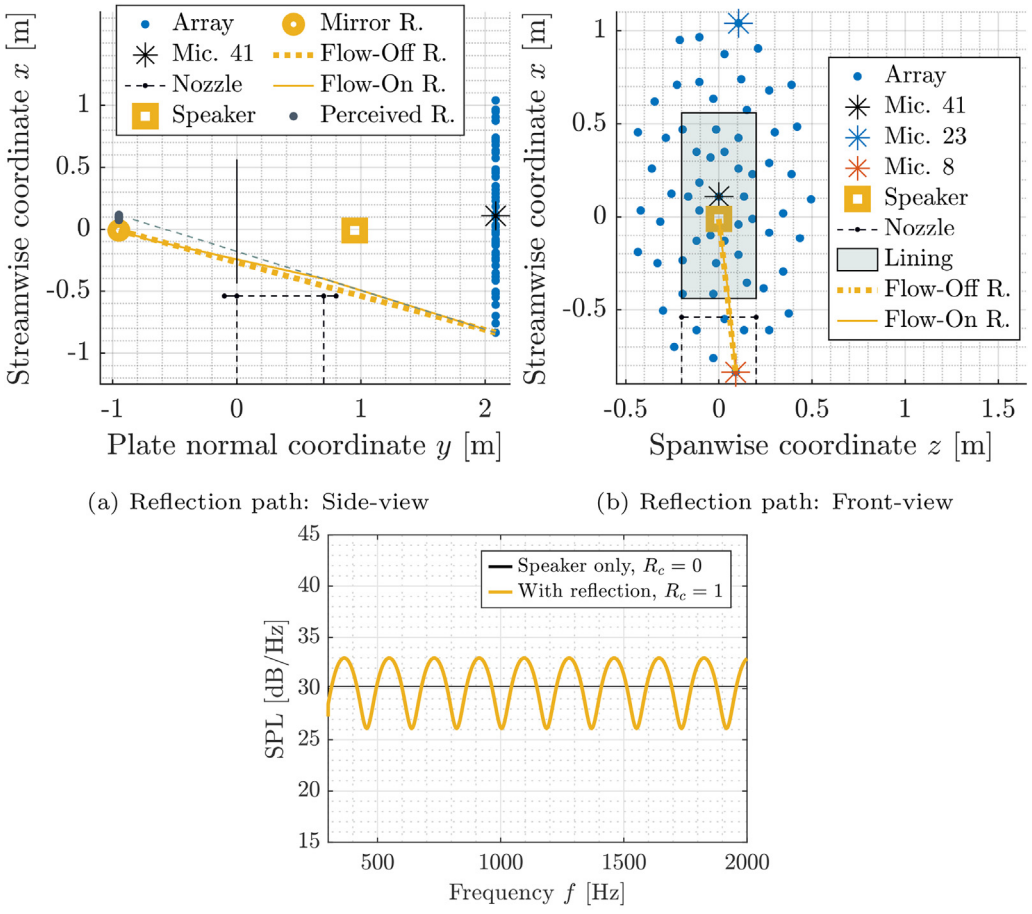

(a) Reflection path: Side-view (b) Reflection path: Front-view

(c) Spectra with and without reflection

Fig. 3. Prediction of the reflections with the geometric modelling tool. Reflection path for the flow-off and -on cases: side-view (top-left) and front-view (top-right). Predicted spectra for the flow-off cases without reflection and with perfect reflection, from the signal simulated for microphone 41, at the array centre (bottom).

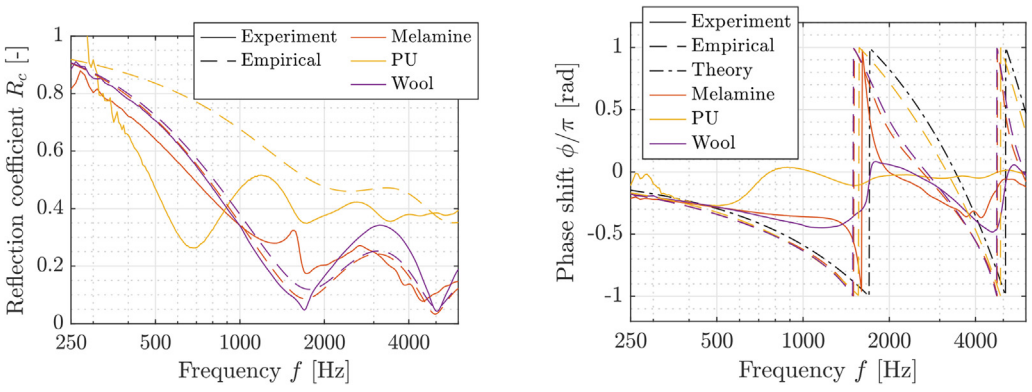

(a) Reflection coefficient (b) Phase shift

Fig. 4. Acoustic characterization of melamine, PU and polyester wool when backed by a solid wall. Experimental data from the impedance tube and empirical data, from Delany's model. Absolute reflection coefficient (left) and phase shift at the surface of the foam (right), considering a normal incidence reflection ($\boldsymbol{\theta_0} = \boldsymbol{0}^\circ$).

on Delany's empirical model for surface impedance [25]. Fig. 4a shows that the empirical model accurately predicts $R_c(f)$ for the melamine and wool linings. For the PU foam, the prediction is very poor at low frequency (around 700 Hz), where the empirical model predicts a stronger reflection. Delany's model makes use of the viscous resistivity for the surface impedance prediction, while neglecting the inertial resistivity. The empirical model is therefore most accurate for predicting the absorption of porous materials when viscous dissipation plays a dominant role. The PU foam has, however, a low viscous resistivity and a very high inertial resistivity (see Table 1), which is in line with the less accurate prediction from the empirical model for this material.

In Fig. 4b, the theoretical phase shift, ϕ, corresponds to the phase shift that occurs, per frequency, for a sound wave which

passes through the material and is fully reflected by the solid back plate:

$$\phi_{\text{Theoretical}} = -2d/\lambda, \tag{8}$$

being d the thickness of the material and λ the wavelength of the sound wave. Fig. 4b shows that the phase shift given by the empirical model is, for all materials, similar to the theoretical. The empirical model therefore assumes that the reflection is almost completely at the solid back plate, identically to the theoretical prediction. This trend is similar to what is indicated by the experimental tests for melamine and wool. However, for the PU foam, the experimental phase shift during the reflection is close to 0, indicating that most of the reflection occurs directly at the surface of the foam. In practice, reflections can occur at two locations: at the surface of the foam and at the solid back wall. However, the impedance tube used in the present investigation only provides a single reflection (or absorption) coefficient. In order to take into account both reflections, it is required to have an estimation of the transmission, absorption and reflection capabilities of the material, for example by testing with a four microphones' impedance tube, as described in [30]. Considering both reflections (on the surface of the material and on the back wall) is expected to have a positive impact on predictions based in the mirror-source method. The present study considers one single reflection. The experimental and empirical reflection coefficients indicate different reflection locations, which influences the frequencies at which acoustic interference occurs, between the direct and the mirror sources (see Fig. 3). Therefore, the comparison of the modelling results allow for the understanding of the impact of the reflection location on the acoustic predictions.

3. Effect of wall treatment on boundary layer aerodynamic characteristics and aerodynamic noise

The present section describes the turbulent boundary layer over the test plates (Section 3.1), and discusses its impact on the spurious aerodynamic noise (Section 3.2). The goal is to characterize the aerodynamic phenomena which can affect noise measurements in a wind tunnel, counter acting the acoustic improvement achieved.

3.1. Turbulent boundary layer characterization

Fig. 5 presents the velocity and turbulence intensity,

$$\text{TI} = u'_{rms}/U_\infty, \tag{9}$$

profiles for the clean and lined plates, measured at locations 0c and 0 l (see Fig. 1c). u'_{rms} is the root mean square of the velocity fluctuations. Fig. 5a also shows the velocity profile at location 3, measured with the clean plate. The shape of the velocity profile does not change along the clean plate, between locations 3 and 0c (0.92 m apart). Fig. 5a highlights the increase in velocity deficit in the boundary layer, as the roughness of the liner increases. In Fig. 5b, turbulence intensity is plotted versus streamwise velocity, in order to remove the error caused by the uncertainty in the distance from the measurement point to the wall [31]. For the roughest plate (wool) the hot-wire was located at least 0.5 mm away from the wool surface, due to the risk of damaging the measurement tool. Fig. 5b shows that the increase in turbulence intensity, with respect to the clean plate, is dominated by the increase in roughness. The differences in viscous and inertial resistivity between the melamine and PU plates are shown to play a negligible role in the velocity and turbulence intensity profiles. The agreement of the measurements at locations 0c and 0 l is indicative of the negligible spanwise variations in boundary layer profiles between the two locations. For a clean plate, a sharp peak in turbulence intensity is expected close to the wall, at $y^+ \approx 15$, being y^+ the non-dimensional wall normal distance [32]. For the rough plates, the peak in turbulence intensity is less sharp and further from the wall [33], and is shown in Fig. 5b. The strong velocity fluctuations caused by the rougher surfaces indicate that these liners can cause stronger background aerodynamic noise, when applied to a closed wind tunnel. Fig. 5 also indicates that the differences in viscous and inertial resistivity between melamine and PU foams (see Table 1) do not considerably affect the turbulent boundary layer properties.

Fig. 6 presents the growth in boundary layer thickness, $\Delta\delta_{99}$, displacement thickness, $\Delta\delta^*$, and momentum thickness, $\Delta\theta$, from the streamwise location where the liner starts, location 2–3 (0.1 m downstream of the nozzle and 0.9 m upstream of location 0c). The boundary layer parameters 0.1 m downstream of the nozzle were obtained from averaging data collected at locations 2 and 3 (clean plate test case), respectively 0.12 m and 0.08 m downstream of the nozzle (see Fig. 1c). Each value is normalised with the growth of the specific boundary layer parameter for the clean plate, from location 2–3 to 0c. For the BL thickness, the normalisation value is:

$$\Delta\delta_{99(\text{Clean,Loc.0c})} = \delta_{99(\text{Clean,Loc.0c})} - \delta_{99(\text{Loc.2-3})}. \tag{10}$$

The clean plate's BL parameters, at the free-stream velocity 30 ms^{-1}, are presented in Table 2. The boundary layer two dimensional friction drag was estimated from:

$$D/b = \rho U_\infty^2 \theta, \tag{11}$$

being b the wall length in the spanwise direction, and ρ the air density.

Fig. 6a shows that the boundary layer thickness is increased as roughness increases, having the wool plate a growth 50% larger than the clean case. At $U_\infty = 20$ ms^{-1} and $U_\infty = 30$ ms^{-1}, the difference in $\Delta\delta^*$ and $\Delta\theta$ between the clean and lined cases approximately doubles, as roughness is increased from ~0.1 mm (melamine and PU) to ~0.6 mm (wool). At the present flow conditions, the rough wall lining materials tested are not expected to affect closed wind tunnel aerodynamic measurements. The changes in the boundary layer parameters are small when compared to the dimensions of closed wind tunnel test sections which are used for aeroacoustics research, e.g. the Low Turbulence Tunnel at TU Delft [1,12]. However, when a liner is applied to a large portion of the wind tunnel's circuit (e.g. lining of diffuser walls in [8]), it is relevant to consider the increase in momentum losses in the circuit. Lining a large portion of the tunnel with a very rough material, such as polyester wool, can lead to a considerable increase in drag of the wind tunnel walls. This would require the tunnel's drive fan to work at a higher power setting. The drive fan is a strong contribution towards background noise in a wind tunnel test section, and can disturb acoustic measurements [34].

Fig. 7 shows the changes in wall pressure fluctuations spectra, caused by the three liners, for the free-stream velocity 30 ms^{-1}. The results from the Sonion microphone of position 0 are in agreement with the spectrum from the Linear-X microphone of position 1 (equal streamwise location), which provides confidence in the result. At low frequency, below 1 kHz, the increase in roughness causes an increase in intensity of the wall pressure fluctuations, which is in line with the higher turbulence intensity seen in Fig. 5b.

According to Manes [21], who measured velocity fluctuations in permeable walls' boundary layers, the frequency band for which the fluctuations are highest becomes narrower as permeability increases, whereas the fluctuations over a smooth plate are distributed over a larger frequency band. In the present study, the plate with highest inertial resistivity (PU) shows a low gradient in the spectrum decay towards higher frequency, as in the impermeable case (clean plate). The materials with high viscous resistiv-

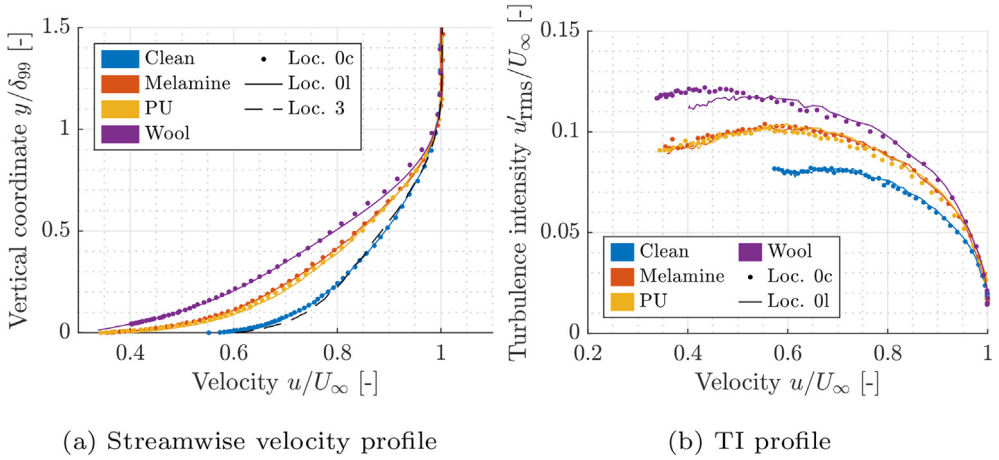

Fig. 5. Boundary layer velocity and turbulence intensity profiles at $\boldsymbol{U}_\infty = 30$ ms^{-1}, 1 m downstream of the nozzle, for the 4 plates tested.

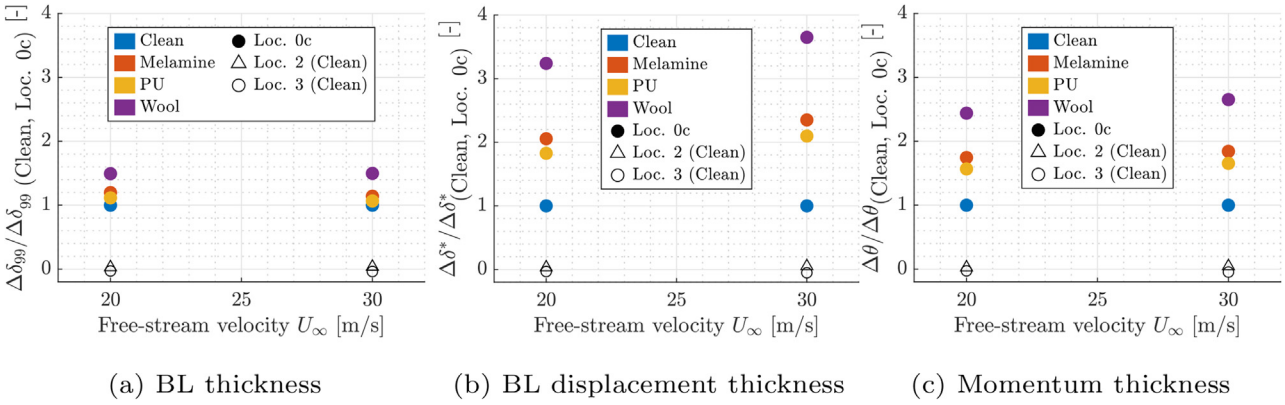

Fig. 6. Effect of the lining materials on BL parameters of the flat plates, 1 m downstream of the nozzle (location 0c). Measurements taken at $\boldsymbol{U}_\infty = 20$ ms^{-1} and $\boldsymbol{U}_\infty = 30$ ms^{-1}. The plots show the BL thickness (left), displacement thickness (centre) and momentum thickness (right).

Table 2
Boundary layer characteristics, for the clean plate case, at $U_\infty = 30$ ms^{-1}.

Location	δ_{99} [mm]	δ^* [mm]	θ [mm]	D/b [N m^{-1}]
2–3	19	2.4	1.9	2.1
0c	31	4.1	3.2	3.6

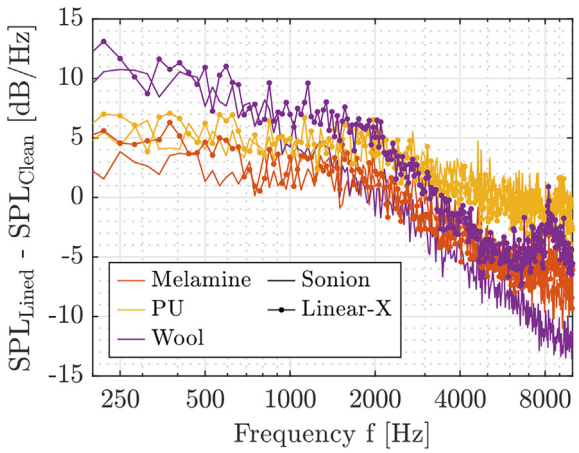

Fig. 7. Spectra of the wall pressure fluctuations at $\boldsymbol{U}_\infty = 30$ ms^{-1}, 1 m downstream of the nozzle. Measurements with a Sonion microphone, at location 0, and with the Linear-X microphone at location 1. SPL difference between the clean plate and the lined plates.

ity and low inertial resistivity (melamine and wool), are observed to result in a faster decay in wall pressure fluctuations' intensity, towards higher frequency, which is in line with the findings presented in [21]. The viscous resistivity of the materials may be associated with a higher dissipation rate of eddies at high frequencies, where the break down of eddies becomes more dominated by viscous forces. To the authors' knowledge, literature is however lacking thorough studies differentiating the effect of viscous and inertial resistivities in the velocity and pressure spectra of turbulent boundary layers, and, consequently, in the spectra of scattered aerodynamic noise. The aerodynamic noise scattered by the four plates is therefore experimentally characterized in the following sub-section.

3.2. Aerodynamic noise sources

The purpose of analysing the aerodynamic noise sources in the experiment is twofold: to identify which properties of the materials lead to a higher aerodynamic noise, and to determine the dominance of the aerodynamic noise levels in the present experiment,

with respect to the speaker noise. The beamforming maps of Fig. 8 show the noise source in the plane of the test plate, for the four plates tested, and for the one-third octave bands centered at 1 kHz and 2 kHz. At 1 kHz, the four maps identify the trailing edge of the plate and the nozzle exit as noise sources. For the clean, melamine and wool plate cases the nozzle and trailing edge noise sources are also visible at 2 kHz.

Following from the discussion of Section 3.1, the boundary layers over the melamine and PU plates are very similar, both in terms of velocity profiles and intensity of the turbulent fluctuations. However, Fig. 8c and g, relative to the PU plate, show higher noise levels than the beamforming maps of the melamine plate (see Fig. 8b and f). At 1 kHz, the intensity of the trailing edge noise is clearly higher for the PU plate. At higher frequency, the figure indicates that the strongest source of noise, for the PU plate case, is originated at the foam surface. The results, therefore, indicate that porous materials with a higher inertial resistivity (see Table 1) result in higher noise scattering, both from a trailing edge and from the porous surface. The higher inertial resistivity of the PU foam (see Table 1) is associated with the higher fibre diameter of this material, which increases the ratio of inertial to viscous forces inside the porous medium [35].

Fig. 9 shows the comparison between speaker noise levels (without flow) and the scattered aerodynamic noise in the flow-on tests. The aerodynamic noise was measured with the speaker off, and for five setup configurations: only wind tunnel nozzle (no plate installed), clean plate (baseline), and for the three lined plates. Fig. 9a presents the spectra averaged over the 64 microphones in the array. The figure shows that the speaker noise is higher than the aerodynamic noise of the configurations tested from approximately 700 Hz. Fig. 9b shows the spectra obtained from source power integration of the beamforming maps, at the source plane. The region of integration is the same as shown in Fig. 8. The speaker noise levels obtained from source power integration are higher than the background noise from 400 Hz, meaning that the beamforming results presented in Section 5 are essentially unaffected by aerodynamic sources.

Fig. 9 highlights the higher aerodynamic noise which is scattered by the PU plate. As indicated by Fig. 8, the PU plate results in both higher trailing edge noise, as well as higher noise from the entire foam surface, resulting from the interaction with the turbulent boundary layer. The results indicate that a porous material with a higher fibre diameter, and consequently a higher inertial resistivity, leads to more aerodynamic noise. The figures indicate that lining materials with a high inertial resistivity should be therefore avoided, in closed wind tunnels.

4. Effect of wall treatment on acoustic source characterization

The present section presents and discusses the acoustic results, which refer to the test cases without flow. The goal of the section is to evaluate the acoustic benefit of the lining materials in a controlled environment. The experimental results are compared with the geometric modelling results for a more complete understanding. The measurements are analysed by considering a single receiver, in Section 4.1, and by analysing the beamforming results, in Section 4.2.

4.1. Single receiver – measurement performance

Fig. 10 shows the acoustic interference caused by the reflection in the measurements by a point receiver. The receiver considered is located at the centre of the array. Fig. 10a shows the simulation results, considering a complete reflection at the location of the foam surface ($R_{c,1} = 1$), a partial reflection at the solid wall behind the foam ($R_{c,2} = 0.5$), and a reflection on a plate lined with melamine, considering the surface reflection coefficient obtained from the impedance tube ($R_{c,1}(f) = R_{\text{Melamine}}$). Fig. 10a shows that, according to the prediction, the lining causes a shift in the frequencies of constructive and destructive interference (positive and negative ΔSPL, respectively). The cases with $R_{c,1}(f) = R_{\text{Melamine}}$ and $R_{c,2} = 0.5$ produce similar results, at low frequencies (between 0.4 and 1 kHz). The result could be expected, since at low frequency the reflection coefficient of the melamine plate is high,

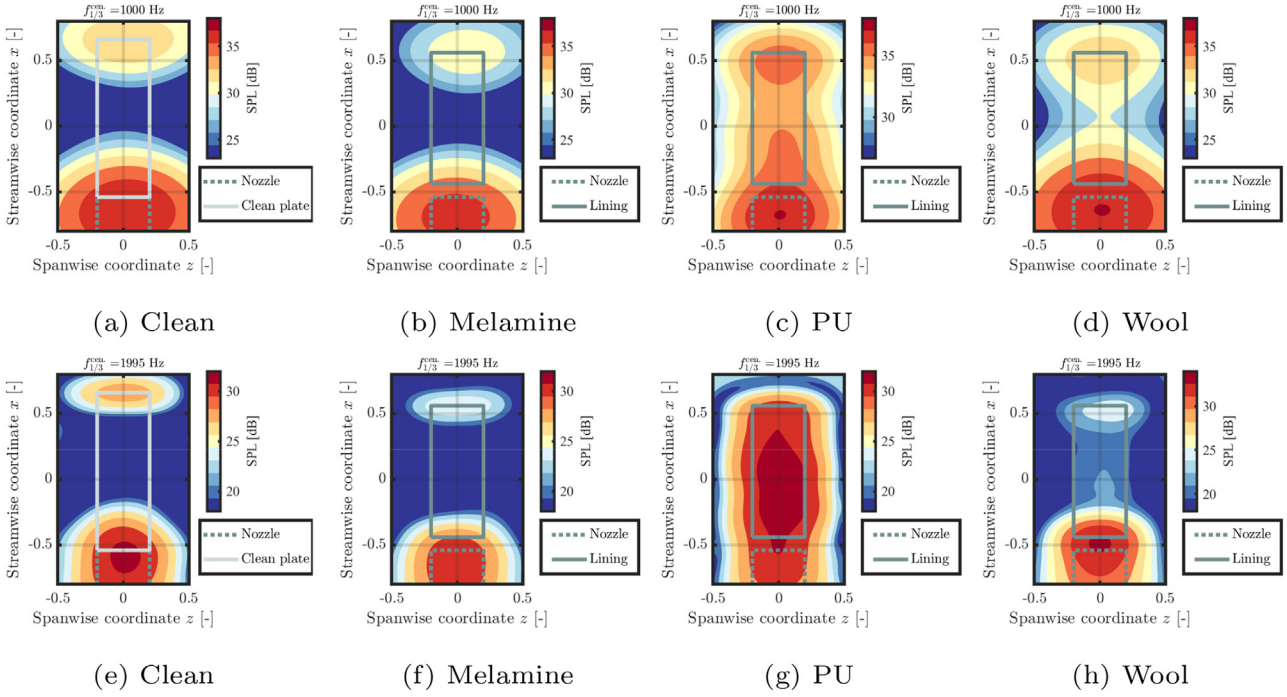

Fig. 8. Beamforming maps at the plate location. Third-Octave bands centered at 1000 Hz (top) and 2000 Hz (bottom). Hard-wall (left) and lined plates (centre-left to right) cases. Free stream velocity, $\boldsymbol{U}_\infty = 30$ ms^{-1}.

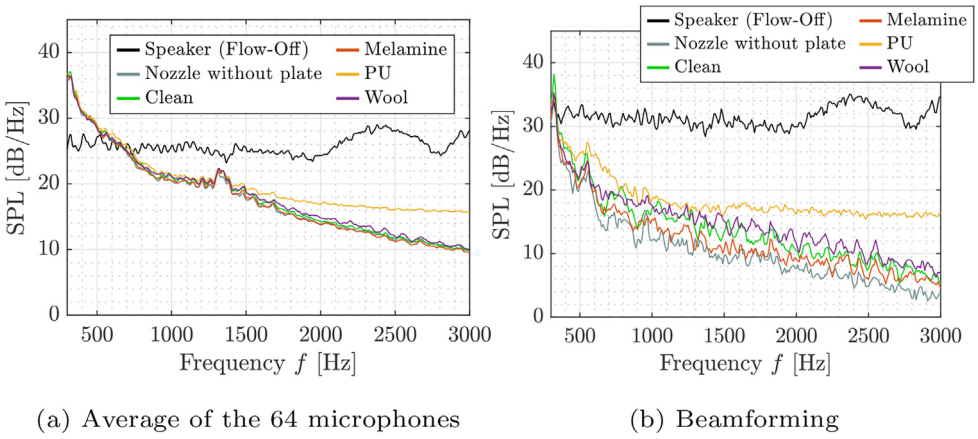

Fig. 9. Comparison between the speaker noise levels (without an installed plate, and without flow) and background noise of the tunnel with the flow-on, at $\boldsymbol{U}_\infty = 30\ \mathrm{ms}^{-1}$. Spectra averaged from the 64 microphones in the array (left); and spectra obtained from SPI at the source plane, from conventional beamforming.

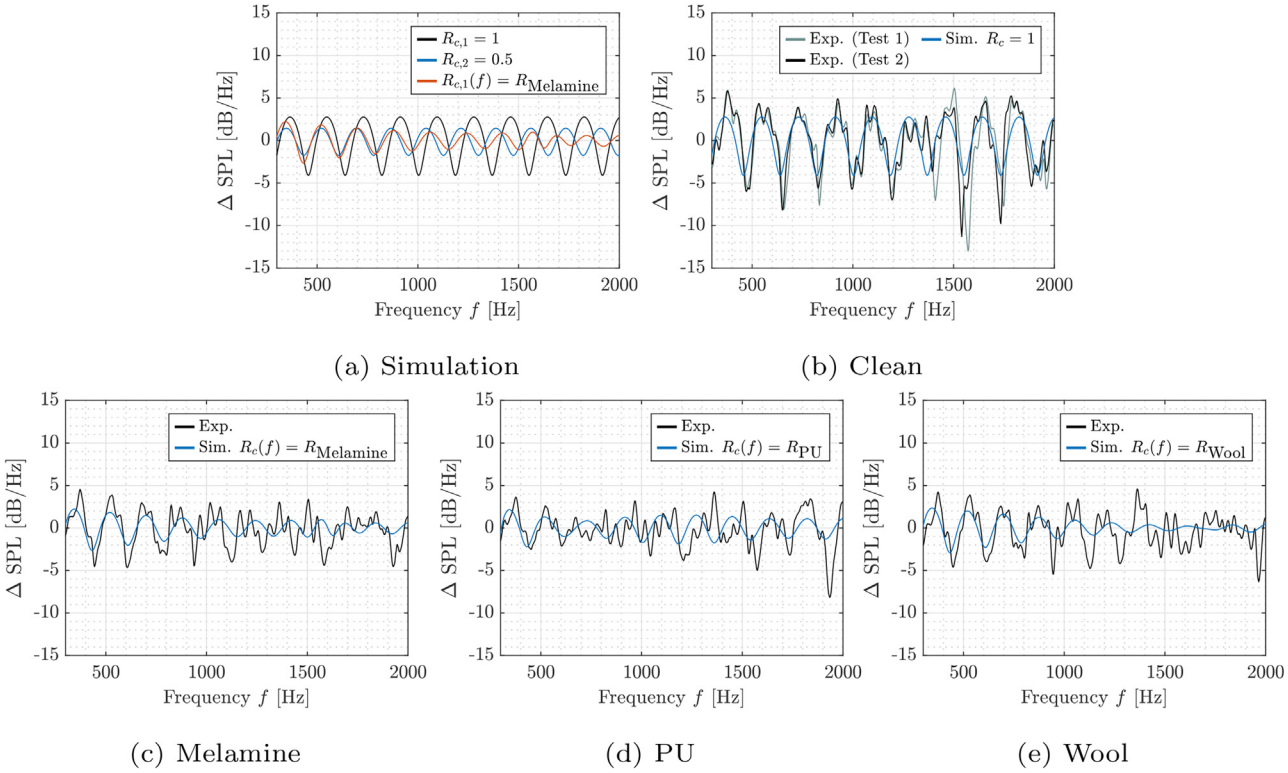

Fig. 10. Acoustic interference caused by a reflection vs. frequency, for a receiver located at the centre of the array (microphone 41). Comparison of simulations, considering different reflections: $\boldsymbol{R_{c,1} = 1, R_{c,2} = 0.5}$ and $\boldsymbol{R_{c,1}(f) = R_{\mathrm{Melamine}}}$ (top-left). Clean plate, measurement and simulation, considering $\boldsymbol{R_{c,1} = 1}$ (top-right). Lined plates, measurement and simulation, considering $\boldsymbol{R_{c,1} = R_{\mathrm{Foam}}}$ (bottom). Reflection coefficient of the lined plates obtained from experimental impedance tube data. Flow-off case, $\boldsymbol{U}_\infty = 0\ \mathrm{ms}^{-1}$.

and also because the reflection occurs mostly at the back plate (from the impedance tube data shown in Fig. 4). The comparison between simulation and clean plate experiment can be seen in Fig. 10b. The results indicate that the mirror-source method is capable of predicting the interference caused by the reflections, with the present setup, for the case of a highly reflective plate. Furthermore, Fig. 10b shows the repeatability of the results, for the acoustic data measured in tests 1 and 2. The two experimental data sets were acquired with 21 days difference.

Fig. 10c–e, compare the simulated and measured spectra for the test cases with the melamine, PU and wool linings, respectively. The results indicate that the algorithm predicts well the frequencies of interference, and the interference levels, for the melamine and wool cases at low frequency (below 1 kHz). At higher frequency, the acoustic absorption of the melamine and wool are high, and the error in the measurement can be dominated by acoustic phenomena not predicted by the geometric modelling tool, e.g. diffuse reflections and diffraction, or noise in the measurement device (see uncertainty in Section 2.2.3). Furthermore, for smaller sound wavelengths, predicting the frequencies of interference can be more challenging, since the result is more prone to inaccuracies, resulting e.g. from an imprecise reflection coefficient obtained from the impedance tube measurements. For the PU foam (Fig. 10d), the simulation provides a reasonable prediction at very

low frequencies. At higher frequencies, i.e. from 0.7 kHz, when R_{PU} is low (see Fig. 4), the experimental result appears to be dominated by noise, e.g. due to diffuse reflections. As discussed in Section 2.3, the fact that only one mirror-source is considered in the simulation can be a source of added errors. It is possible that, at certain frequencies, the reflections at the foam surface and at the back plate can have constructive or destructive interference with each other, at the receiver location.

4.2. Beamforming performance

Fig. 11 presents conventional beamforming maps, at the source plane, for the simulated and experimental cases of a free-field speaker (Fig. 11a and d), speaker with a highly reflective back wall installed (Fig. 11b and e), and speaker with a melamine plate installed (Fig. 11c and f). The results show that the difference between the beamforming maps is negligible, when the purpose is to locate the position of the direct source in the scan plane. The next step was to apply source power integration in a region close to the source, in order to evaluate the consequence of installing a back wall in the assessment of the source noise levels. The integration area is specified in Fig. 11.

The ΔSPL in source level estimation with source power integration caused by the reflections is presented in Fig. 12. Fig. 12a presents the results for the simulated signals. Fig. 12a compares the ΔSPL when a single receiver is considered (in this case microphone 41) to the error when the spectrum is obtained from source power integration. The results indicate that beamforming is capable of largely reducing the error caused by the back plate reflection, particularly at high frequency, close to 2 kHz. The agreement in Fig. 12b indicates that the geometric modelling tool is capable of predicting the performance of beamforming when the back plate is highly reflective (case without lining).

Fig. 12c–e, show that the geometric modelling tool is capable of incorporating the complex reflection coefficient of the materials. The prediction is particularly good at low frequency, when the performance of geometric modelling tools is most uncertain, as the ratio between setup geometry sizes and sound wavelength reduces [13]. Fig. 12c–e show the simulated spectra obtained using both the experimental and empirical reflection coefficients (see Fig. 4). The results for the melamine and wool cases indicate a slight improvement in the prediction at high frequency (above 1 kHz), when the empirical reflection coefficient is used. The result therefore indicates that most of the reflection occurs at the back solid wall, as predicted by Delany's empirical model (see Fig. 4). For the PU plate, however, both the magnitude of the peaks and the frequencies of interference are more accurately predicted when the experimental impedance tube data is used. As discussed in Section 2.3, Delany's model only takes into account the viscous resistivity, whereas the PU foam has a very high inertial resistivity (see Table 1). The reflection location is therefore mispredicted by the empirical model, resulting in errors in the prediction of the interference between direct source and reflections. Fig. 12 is indicative of the importance of knowing the exact reflection location, when using a geometric modelling tool.

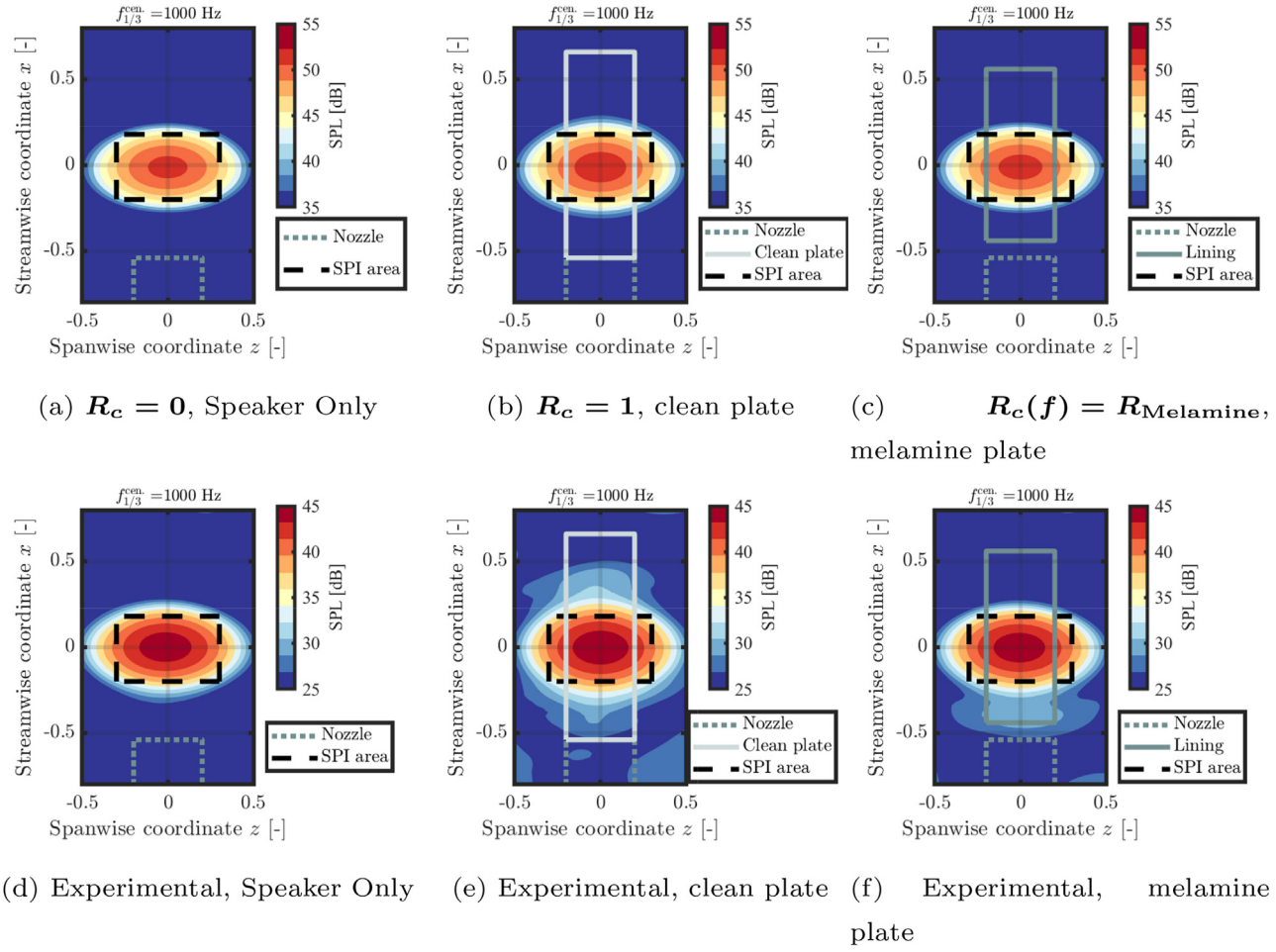

Fig. 11. Beamforming of the simulated (top) and experimental (bottom) microphone signals, at the source plane. The maps are for the 1000 Hz third-octave band. Free-field speaker case (left), speaker with the clean plate installed (centre), and speaker with a melamine plate installed (right). Flow-off case, $\boldsymbol{U}_\infty = 0$ ms^{-1}.

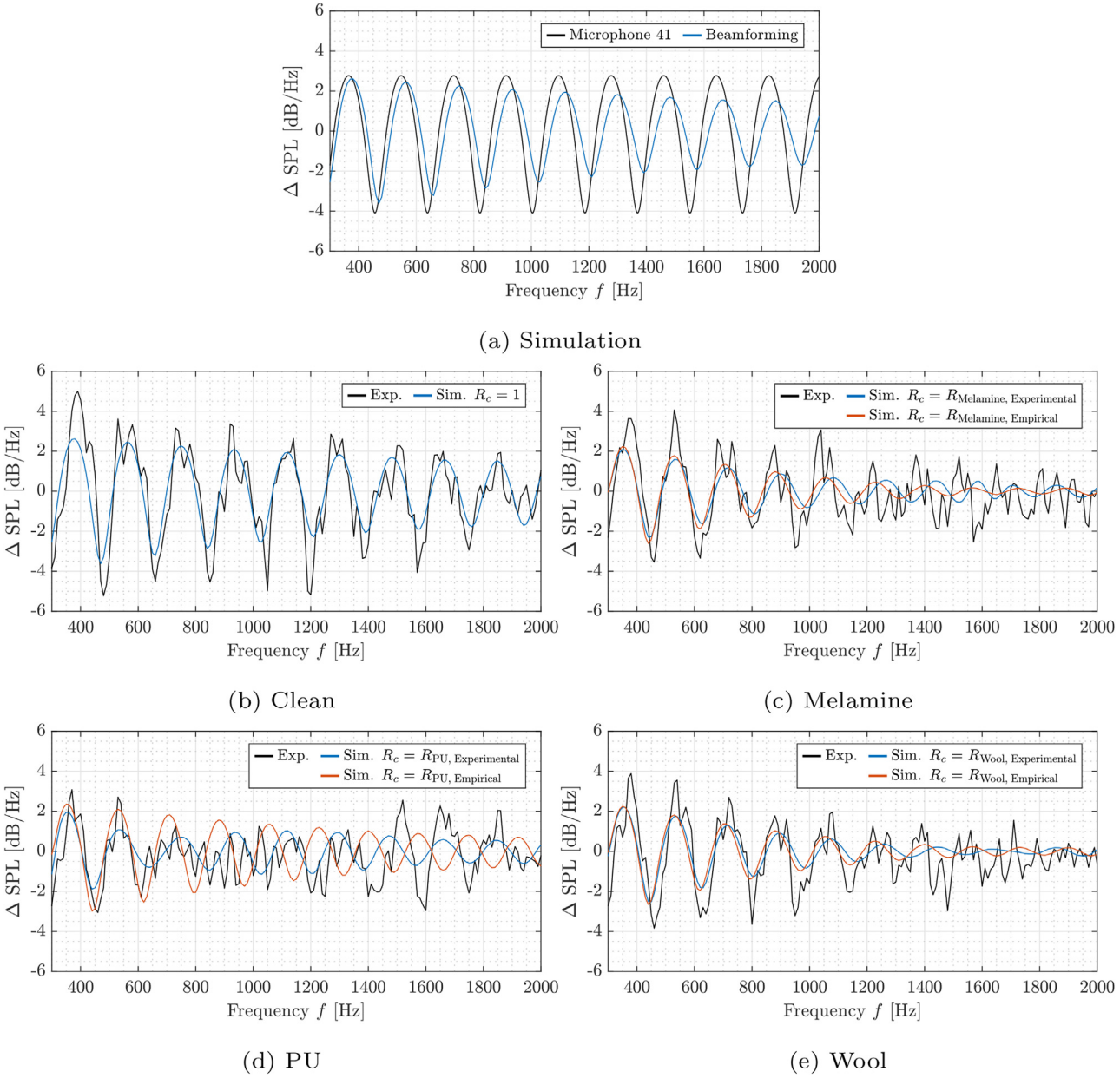

Fig. 12. Acoustic interference caused by a reflection vs. frequency. Simulation: isolated microphone (41) and beamforming spectra (top-left). Beamforming of experimental data with the clean plate and beamforming of the simulated data, with $\boldsymbol{R_c} = \boldsymbol{1}$ (top-right). Beamforming of experimental data with the lined plates and beamforming of the simulated data (bottom). Results obtained from Source Power Integration of the beamforming maps. Flow-off case, $\boldsymbol{U}_\infty = 0$ ms^{-1}.

5. Acoustic wave – flow interaction: flow-on reflection prediction

The present section discusses the interaction between the acoustic reflected wave and flow, and its effect on the acoustic measurements. To this end, Section 5.1 discusses the effect of the flow in the measurements from isolated receivers, and Section 5.2 describes the consequence of the interaction between acoustic wave and flow in the beamforming results.

5.1. Single microphone

Fig. 13 presents the acoustic interference occurring during the measurement of the speaker noise levels, due to the reflection, for the flow-off and -on cases. Both the experimental and the simulated results are shown. The data was obtained by three isolated receivers: microphone 8, at the bottom of the array, microphone 23, at the top of the array, and microphone 41, at the centre of the array (see Fig. 3b). The simulation predicts that, when the reflected wave is convected by the flow, the receiver sees a shift in the frequencies of interference between the direct and reflected sound waves. The flow convection influences the travel time of the reflected wave, from source to receiver. The shift in frequency depends on the location of the receiver. For receivers located below the speaker, e.g. microphone 8, the reflected wave is convected in the opposite direction of its path, and takes longer to reach the receiver. The frequencies of interference therefore shift towards lower frequency at the location of microphone 8, when the flow is on. For a receiver above the speaker, however, the convection of the reflected wave reduces the sound wave's travelling time.

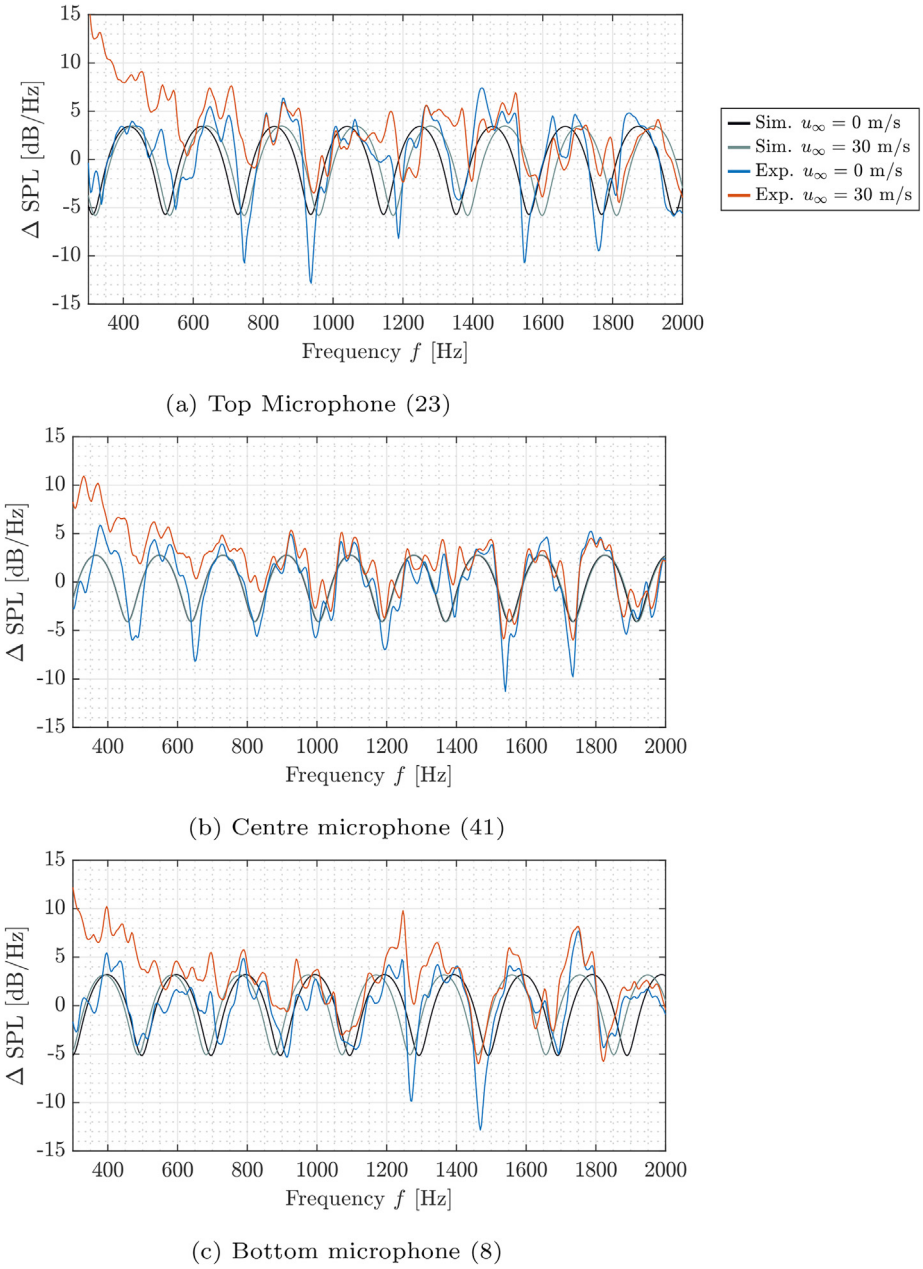

Fig. 13. Acoustic interference caused by a reflection (and aerodynamic noise) vs. frequency, as perceived by isolated receivers. Comparison between simulation with flow-off and -on, and experiment with flow-off and -on. Microphones at the bottom of the array (left), at the middle of the array (centre) and at the top of the array (right). Clean plate test case, at the free stream velocity, $\boldsymbol{U}_\infty = 30$ ms^{-1}.

Microphone 23, therefore, sees a shift in the frequencies of interference towards higher frequency, as the flow velocity is increased. For receivers at a height close to the speaker height, the travel time of the reflected wave is essentially unchanged by flow convection, at the velocities considered. Microphone 41, at the centre of the array, is predicted to perceive equal interference between the reflected and direct sound waves, at the free-stream velocities 0 ms^{-1} and 30 ms^{-1}.

The experimental data in Fig. 13 shows very similar results for the 0 ms^{-1} and 30 ms^{-1} case, from 700 Hz. Below 700 Hz, the results for the 30 ms^{-1} case are dominated by background aerodynamic noise, as indicated by the results of Section 3.2. Fig. 13a and c show a slight shift in the frequencies of interference in the experimental data, as indicated by the geometric modelling prediction. However, the experimental shift is very small compared to the noise in the results. The following subsection analyses data from all the microphones in the array, which helps reducing the influence of spurious acoustic noise sources, e.g. diffuse reflections.

5.2. Conventional beamforming

Fig. 14 shows the error caused by acoustic interference in the beamforming estimate of the speaker levels, for the flow-off and -on cases. The spectra were obtained from source power integration of the beamforming maps, with an equal scan plane and region of integration as in Fig. 11. The figure shows that, according to the simulation, the presence of the flow does not affect the beamforming results in the present setup. The result is aligned with the discussion of the previous sub-section (Section 5.1), where it was referred that the flow causes a shift in the frequencies of interference, which is dependent on the position of the receiver. Since the 64 microphones are approximately equally spread above and

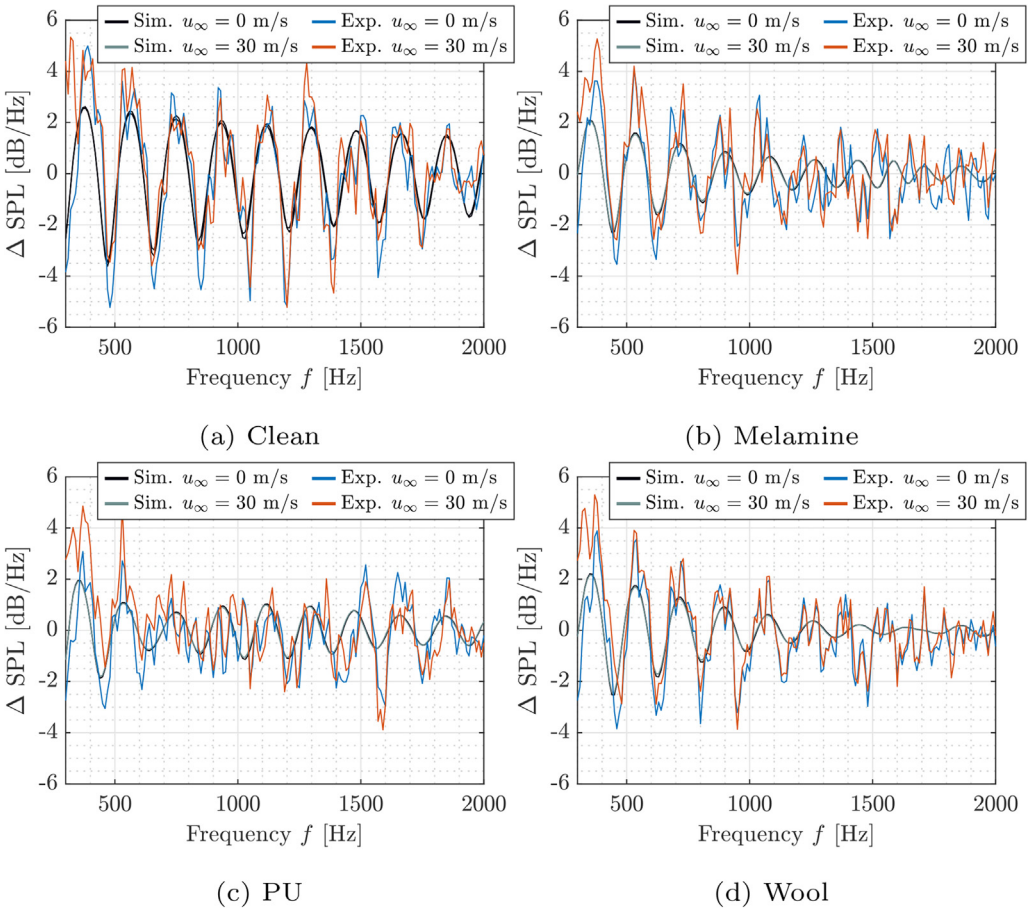

Fig. 14. Acoustic interference caused by a reflection, in the spectra obtained from beamforming. Comparison between the flow-off and -on ($\boldsymbol{U}_\infty = 30$ ms^{-1}) cases. Spectra obtained from SPI of the beamforming maps at the source plane. Experimental and simulated data relative to the clean (top-left) and lined plates (top-right and bottom). Reflection coefficient of the lined plates obtained from experimental impedance tube data.

below the speaker (see Fig. 3), when all the microphones are considered, the shift in frequency of interference becomes negligible. The experimental results presented in Fig. 14b–e correspond to the test cases with the clean, melamine, PU and wool plates, respectively. The experimental results are in agreement with the predictions, since the difference in experimental spectra at 0 ms^{-1} and 30 ms^{-1} is also negligible. Small differences can be seen at very low frequency, below 500 Hz, due to aerodynamic background noise. Considering the frequencies 500 Hz $< f <$ 2000 Hz, the correlation between the spectra with and without flow is high for the 4 plates tested. The correlation coefficient is 0.8, 0.7, 0.6 and 0.9 for the clean, melamine, PU and wool test cases, respectively. The results are therefore indicative that flow phenomena which are neglected by the geometric modelling tool, such as transmission loss or refraction in shear layers, play a minor influence in the experiment carried out in the A-tunnel. As discussed in Section 4.2, a good estimation of the location of the reflections, which can be at the surface of the foam or at the solid back wall, is a dominant factor for an accurate prediction of the geometric modelling algorithm. Fig. 14 shows that, also for the flow-on cases, the interference peaks are approximately predicted by the geometric modelling algorithm, as long as the reflection coefficient of the back wall is sufficiently high, i.e. $R_c(f) > 0.4$ (see Fig. 4). For frequencies where the reflection coefficient is low, the result becomes dominated by spurious noise, which can be associated with diffuse reflections and diffraction. When beamforming is applied, the convection of a reflected wave by the flow can be neglected, as long as the direct sound source is (approximately) aligned with the centre of the microphone array.

6. Conclusion

An experimental campaign was carried out in an anechoic open-jet wind tunnel, in order to evaluate the influence of lining materials on the aerodynamic and acoustic fidelity of wind tunnel test sections. The test models consisted of plates lined with sound absorbing porous materials. The porous materials were characterized based on their surface roughness, viscous and inertial resistivities, and reflection coefficient. The study focuses on the influence of the liners on the boundary layer of the wind tunnel's wall, on the boundary layer aerodynamic noise, and on the absorption of sound reflections. A geometric modelling algorithm was developed in order to improve the understanding of the effect of lining the wind tunnel wall on the acoustic measurements.

For the flow-on tests, the aerodynamic properties of the boundary layer of each test plate were initially characterized. The turbulent fluctuations in the boundary layer where confirmed to be most increased for the roughest material tested, polyester wool, particularly at low frequencies. However, it was the lining material with largest fibre diameter (PU), and consequently higher inertial resistivity, which was found to scatter most aerodynamic noise, both from the surface and from the trailing edge.

During the acoustic tests, a well characterized speaker was placed in front of the lined wall. Measurements were taken with

a phased acoustic array. The results show that the modelling algorithm is capable of predicting the interference caused by acoustic reflections, for the clean wall and lined cases. For the lined cases, however, at high frequencies, when the absorption from the lining materials is increased, acoustic spurious noise sources become more dominant in the experimental data. Both the geometric modelling algorithm and the experiments show that the highest improvement on the acoustic measurements occurs for the lining materials with highest viscous resistivity, melamine and wool, due to their increased sound absorption capabilities. The results indicate that the best choice of acoustic lining material, for a closed wind tunnel, results from maximizing viscous resistivity, while reducing roughness and inertial resistivity.

The present study highlighted the advantages and limitations of porous wind tunnel lining materials with varying roughness, viscous resistivity and inertial resistivity. The capabilities of a geometric modelling tool to predict the acoustic benefit of each lining material was also accessed. Future aeroacoustic investigations would benefit from the validation of geometric modelling methods in closed wind tunnel environments, with walls lined with sound absorbing materials. The presence of the wind tunnel walls perpendicular to the array increase the amount of specular and diffuse reflections, increasing the complexity of the acoustic problem.

CRediT authorship contribution statement

Hugo F.M. Bento: Conceptualization, Methodology, Software, Validation, Formal analysis, Investigation, Writing – original draft, Visualization. **Daniele Ragni:** Conceptualization, Methodology, Writing – review & editing, Supervision, Project administration, Funding acquisition. **Francesco Avallone:** Conceptualization, Methodology, Writing – review & editing, Supervision, Funding acquisition. **Dick Simons:** Writing – review & editing, Supervision. **Mirjam Snellen:** Conceptualization, Methodology, Writing – review & editing, Supervision, Project administration, Funding acquisition.

Declaration of Competing Interest

The authors declare that they have no known competing financial interests or personal relationships that could have appeared to influence the work reported in this paper.

Acknowledgments

The research is inserted within the framework of the NWO-TTW THAMES (Towards High-Reynolds Airfoil self-noise MEasurementS) project, with Grant No. 15215. The authors would like to acknowledge the users of the project, and in particular Pieter Sijtsma, for the valuable insight on the results. The contribution of the Netherlands Aerospace Centre (NLR), by performing the impedance tube tests, was essential. For this, the authors very much appreciate the collaboration with Marthijn Tuinstra. The authors would also like to thank Steve van Herk, for the help preparing the experimental setup, and Christopher Teruna, for the help during the campaign.

References

[1] Merino-Martinez R, van der Velden W, Avallone F, Ragni D. Acoustic measurements of a DU96-W-180 airfoil with flow- misaligned serrations at a high Reynolds number in a closed- section wind tunnel. In 7th International Conference on Wind Turbine Noise Rotterdam, no. May; 2017.

[2] Rubio Carpio A, Merino Martínez R, Avallone F, Ragni D, Snellen M, van der Zwaag S. Experimental characterization of the turbulent boundary layer over a porous trailing edge for noise abatement. J Sound Vib 2019;443:537–58. https://doi.org/10.1016/j.jsv.2018.12.010.

[3] Sinnige T, Ragni D, Malgoezar AM, Eitelberg G, Veldhuis LL. APIAN-INF: an aerodynamic and aeroacoustic investigation of pylon-interaction effects for pusher propellers. Tech. Rep. 2018;2. https://doi.org/10.1007/s13272-017-0247-2.

[4] Cattafesta L, Bahr C, Mathew J. Fundamentals of Wind-Tunnel Design. Encyclopedia Aerospace Eng 2010:1–10. https://doi.org/10.1002/9780470686652.eae532.

[5] Devenport WJ, Burdisso RA, Borgoltz A, Ravetta PA, Barone MF, Brown KA, Morton MA. The Kevlar-walled anechoic wind tunnel. J Sound Vib 2013;332(17):3971–91. https://doi.org/10.1016/j.jsv.2013.02.043.

[6] Blacodon D, Bulté J. Reverberation cancellation in a closed test section of a wind tunnel using a multi-microphone cesptral method. J Sound Vib 2014;333(9):2669–87. https://doi.org/10.1016/j.jsv.2013.12.012.

[7] Schultz TJ. Acoustics of the concert hall. IEEE Spectr 1965;2(6):56–67. https://doi.org/10.1109/MSPEC.1965.5531663.

[8] Remillieux MC, Crede ED, Camargo HE, Burdisso RA, Devenport WJ, Rasnick M, Van Seeters P, Chou A. Calibration and demonstration of the new Virginia Tech anechoic wind tunnel. In: 14th AIAA/CEAS Aeroacoustics Conference (29th AIAA Aeroacoustics Conference). https://doi.org/10.2514/6.2008-2911.

[9] Soderman PT, Schmitz FH, Allen CS, Jaeger SM, Sacco JN, Hayes JA. Design of a deep acoustic lining for the 40- by 80- Foot Wind Tunnel test section. In 5th AIAA/CEAS Aeroacoustics Conference and Exhibit, no. c, 1999. pp. 899–918. doi:10.2514/6.1999-1938.

[10] Merino-Martínez R, Sijtsma P, Snellen M, Ahlefeldt T, Antoni J, Bahr CJ, Blacodon D, Ernst D, Finez A, Funke S, Geyer TF, Haxter S, Herold G, Huang X, Humphreys WM, Leclère Q, Malgoezar A, Michel U, Padois T, Pereira A, Picard C, Sarradj E, Siller H, Simons DG, Spehr C. A review of acoustic imaging methods using phased microphone arrays: Part of the Aircraft Noise Generation and Assessment Special Issue, vol. 10. Vienna: Springer; 2019. https://doi.org/10.1007/s13272-019-00383-4.

[11] Luesutthiviboon S, Malgoezar AM, Merino-Martinez R, Snellen M, Sijtsma P, Simons DG. Enhanced HR-CLEAN-SC for resolving multiple closely spaced sound sources. Int J Aeroacoust 2019;18(4–5):392–413. https://doi.org/10.1177/1475472X19852938.

[12] VanDercreek CP, Amiri-Simkooei A, Snellen M, Ragni D. Experimental design and stochastic modeling of hydrodynamic wave propagation within cavities for wind tunnel acoustic measurements. Int J Aeroacoust 2019;18(8):752–79. https://doi.org/10.1177/1475472X19889949.

[13] Savioja L, Svensson UP. Overview of geometrical room acoustic modeling techniques. J Acoust Soc Am 2015;138(2):708–30. https://doi.org/10.1121/1.4926438.

[14] Hodgson M. On the accuracy of models for predicting sound propagation in fitted rooms. J Acoust Soc Am 1990;88(2):871–8. https://doi.org/10.1121/1.399737.

[15] Lehmann EA, Johansson AM, Nordholm S. Reverberation-time prediction method for room impulse responses simulated with the image-source model. IEEE Workshop Appl Signal Process Audio Acoust 2007;1:159–62. https://doi.org/10.1109/ASPAA.2007.4392980.

[16] Fischer J, Doolan C. Beamforming in a reverberant environment using numerical and experimental steering vector formulations. Mech Syst Signal Process 2017;91:10–22. https://doi.org/10.1016/j.ymssp.2016.12.025.

[17] Mimani A, Porteous R, Doolan CJ. A simulation-based analysis of the effect of a reflecting surface on aeroacoustic time-reversal source characterization and comparison with beamforming. Wave Motion 2017;70:65–89. https://doi.org/10.1016/j.wavemoti.2016.06.003.

[18] Guidati S, Guidati G, Wagner S. Beamforming in a reverberating environment with the use of measured steering vectors. In 7th AIAA/CEAS Aeroacoustics Conference and Exhibit (May). doi:10.2514/6.2001-2166.

[19] Fenech BA, Takeda K. Towards more accurate beamforming levels in closed-section wind tunnels via de-reverberation. In: 13th AIAA/CEAS Aeroacoustics Conference (28th AIAA Aeroacoustics Conference). p. 1–12. https://doi.org/10.2514/6.2007-3431.

[20] Howe MS. Surface pressures and sound produced by turbulent flow over smooth and rough walls. J Acoust Soc Am 1991;90(2):1041–7. https://doi.org/10.1121/1.402292.

[21] Manes C, Poggi D, Ridolfi L. Turbulent boundary layers over permeable walls: Scaling and near-wall structure. J Fluid Mech 2011;687:141–70. https://doi.org/10.1017/jfm.2011.329.

[22] Suga K, Matsumura Y, Ashitaka Y, Tominaga S, Kaneda M. Effects of wall permeability on turbulence. Int J Heat Fluid Flow 2010;31(6):974–84. https://doi.org/10.1016/j.ijheatfluidflow.2010.02.023.

[23] Merino-Martínez R, Rubio Carpio A, Lima Pereira LT, van Herk S, Avallone F, Ragni D, Kotsonis M. Aeroacoustic design and characterization of the 3D-printed, open-jet, anechoic wind tunnel of Delft University of Technology. Appl Acoust 170. doi:10.1016/j.apacoust.2020.107504.

[24] ISO 25178-2:2012. Geometrical Product Specifications (GPS)–Surface Texture: Areal-Part 2: Terms, Definitions and Surface Texture Parameters, International Standards Organization.

[25] Delany ME, Bazley EN. Acoustical properties of fibrous absorbent materials. Appl Acoust 1970;3(2):105–16. https://doi.org/10.1016/0003-682X(70)90031-9.

[26] GRAS Sound & Vibration, Gras 40ph, CCP Free-field Array Microphone (Accessed online 2021–10-05). URL: https://www.grasacoustics.com/

products/special-microphone/array-microphones/product/ss_export/pdf2?product_id=178.
[27] Luesutthiviboon S, Malgoezar A, Snellen M, Sijtsma P, Simons D. Improving source discrimination performance by using an optimized acoustic array and adaptive high-resolution CLEAN-SC beamforming. 7th Berlin Beamforming Conference 2018:1–26.
[28] Sijtsma P. Phased Array Beamforming Applied to Wind Tunnel and Fly-Over Tests. In SAE Technical Papers, Vol. 2010-Octob, 2010. pp. 17–19. doi:10.4271/2010-36-0514.
[29] Aretz M, Dietrich P, Vorländer M. Application of the mirror source method for low frequency sound prediction in rectangular rooms. Acta Acust United Acust 2014;100(2):306–19. https://doi.org/10.3813/AAA.918710.
[30] Koruk H, Genc G. Acoustic and mechanical properties of luffa fiber-reinforced biocomposites. Elsevier Ltd 2018. https://doi.org/10.1016/B978-0-08-102292-4.00017-5.
[31] Alfredsson PH, Örlü R. The diagnostic plot a litmus test for wall bounded turbulence data. Eur J Mech B/Fluids 2010;29(6):403–6. https://doi.org/10.1016/j.euromechflu.2010.07.006.
[32] Marusic I, Kunkel GJ. Streamwise turbulence intensity formulation for flat-plate boundary layers. Phys Fluids 2003;15(8):2461–4. https://doi.org/10.1063/1.1589014.
[33] Jiménez J. Turbulent flows over rough walls. Annu Rev Fluid Mech 2004;36(1991):173–96. https://doi.org/10.1146/annurev.fluid.36.050802.122103.
[34] Gomes JP, Bergmann A, Holthusen H. Aeroacoustic wind tunnel design. CEAS Aeronaut J 2019;10(1):231–49. https://doi.org/10.1007/s13272-019-00372-7.
[35] Hersh AS, Walker B. Acoustic Behavior of Fibrous Bulk Materials. AIAA Paper 1980. https://doi.org/10.2514/6.1980-986.